DETC2023-109120

ZERO PARASITIC SHIFT PIVOTING KINEMATIC STRUCTURES BASED ON COUPLED N-RRR PLANAR PARALLEL MECHANISMS FOR FLEXURE PIVOT DESIGN

Loïc Tissot-Daguette[1], Etienne Thalmann[1], Florent Cosandier[1], Simon Henein[1]

[1]Micromechanical and Horological Design Laboratory (Instant-Lab), EPFL, Neuchâtel, Switzerland

ABSTRACT

Flexure pivots, which are widely used for precision mechanisms, generally have the drawback of presenting parasitic shifts accompanying their rotation. The known solutions for canceling these undesirable parasitic translations usually induce a loss in radial stiffness, a reduction of the angular stoke, and a nonlinear moment-angle characteristics. This article introduces a novel family of kinematic structures based on coupled n-RRR planar parallel mechanisms which presents exact zero parasitic shifts, while alleviating the drawbacks of some known pivoting structures. Based on this invention, three symmetrical architectures have been designed and implemented as flexure-based pivots. The performance of the newly introduced pivots has been compared via Finite Element models with that of two known planar flexure pivots having theoretically zero parasitic shift. The results show that the newly introduced flexure pivots are an order of magnitude radially stiffer than the considered pivots from the state of the art, while having zero parasitic shift properties and equivalent angular strokes. These advantages are key to applications such as mechanical time bases, surgical robotics, or optomechanical mechanisms. Polymer mockups and a titanium alloy prototype have been manufactured for future experimental validation.

Keywords: Flexure pivot, Remote center of motion, Stiffness nonlinearity, Radial stiffness, Parasitic shift

1. INTRODUCTION

Flexure pivots are commonly used in precision mechanisms as they can provide an accurate and repeatable rotation of mechanical elements. Their absence of solid friction, wear, lubrification and backlash and the possibility of monolithic manufacturing makes flexure pivots highly beneficial for micro- and nanopositioning systems [1-4], surgical instruments [5-7], space applications [8-10] and horological oscillators [11-14].

In high precision applications, flexure pivots must achieve a motion of the rotating part as close as possible to a pure rotation. Indeed, several of the known flexure pivots exhibit parasitic shifts in addition to the desired rotational motion. This defect is generally quantified by measuring the parasitic center shift of the pivot, which is the displacement of the point lying on the initial rotation axis and belonging to the rotating part of the pivot. Most flexure pivots, such as cross-spring pivots, have a parasitic shift which can be expanded by a second order power series with respect to the angular stroke. For specific geometries or structures, it is possible to minimize this second order term [14-17]. For instance, the parasitic center shift of a cross-spring pivot is minimized if the crossing axis coincides at ~12.73% of the length of the beams [18].

A theoretically zero parasitic shift can be obtained for flexure pivots with rotational symmetry [9,19,20]. Nevertheless, most designs are either: underconstrained [4,9,21], implying internal vibrations; overcontrained [4,20], which can create a highly unpredictable restoring torque and a limited rotation angle; or non-planar [9,20], requiring assembly which can induce large assembly errors. Today, the only known rotationally symmetric pivot without underconstraint and slightly overcontrained is the triple crossed flexure named TRIVOT [19]. Nevertheless, its radial support stiffness appears to be relatively low [22].

Depending on the application, the support stiffness of the pivot must be as high as possible [23]. Thus, the motion of the pivot does not depend on external loads applied to this pivot, such as gravity or linear accelerations. For flexure pivots whose structure is planar, the support stiffness is evaluated by its radial stiffness, since the out-of-plane stiffnesses are mostly dependent on the structure height. It was shown in Ref. [22] that the radial stiffness can be increased if the thickness of secondary flexures (i.e., flexures having a second order motion with respect to the applied angle) is increased. However, this also increases the nonlinearity of the moment-angle characteristics of the pivot. This nonlinearity lowers the angular stroke of the pivot and can be undesired for some applications. For instance, the rotation stiffness nonlinearity of time base flexure pivot oscillators must be as low as possible to minimize the isochronism defect (i.e., the change of frequency of the oscillator with amplitude) [11,14].

In this paper, we present a new family of planar flexure pivot designs, based on RRR planar parallel manipulators with

kinematic chain coupling, having theoretically no parasitic shift and a high radial stiffness (patent pending [24]). They aim at fulfilling the same function as classic cross-spring pivots, i.e., to provide a rotational motion using flexures, but with advantageous characteristics. In asymmetrical configurations, these mechanisms exhibit a rotation which is about a remote center of motion (RCM), making them highly beneficial for minimally invasive surgery (MIS) robotics and tool holders [25]. When designed with a rotational symmetry, the pivots are largely insensitive to the gravity orientation, which is particularly essential for horological applications [14,26,27]. The kinematics and the flexure implementations of these pivots are respectively described in Sections 2 and 3. Their performances are compared to existing planar flexure pivots in Section 4 using Finite Element Modeling (FEM). The FEM results, exposed in Section 6, allow us to conclude in Section 7 that these new flexure pivots have a negligible parasitic shift of the center of rotation. Furthermore, they exhibit superior performances over existing flexure pivots in terms of radial stiffness.

2. DESCRIPTION OF THE N-RRR PIVOT FAMILY

The pivots presented in this article are based on two generic architectures that we call Type I and Type II pivots. All declinations of these architectures are based on three or more kinematic chains ($n \geq 3$) based on three serial revolute joints (RRR) connecting in parallel the rotating platform to the fixed base. We thus gave the name n-RRR Pivot to this family of pivots. The individual architectures are then given names such as TRIOVOT ($n = 3$), QUADRIVOT ($n = 4$) and HEXAVOT ($n = 6$). Based on these particular cases, it is straightforward to conceive other pivots of the same family having other n values.

2.1 Generic Type I Pivots
2.1.1 Topology

A Type I pivot is presented in Fig. 1c. It is composed of a mobile platform (PF) connected via three main revolute joints (A_1, A_2 and A_3) to three main rigid links (ML1, ML2 and ML3). These three main links are connected via three intermediate revolute joints (B_1, B_2 and B_3) to three secondary rigid links (SL1, SL2 and SL3) respectively. The three secondary links are connected to the fixed base via three secondary revolute joints (C_1, C_2 and C_3). The secondary links SL1 and SL2 are connected to each other via a rigid coupling link CL1 and two coupling revolute joints D_{11}, D_{12}. The secondary links SL2 and SL3 are connected to each other via a rigid coupling link CL2 and two coupling revolute joints D_{21} and D_{22}. The geometry is built around a point O called the *center* of the mechanism.

Remark 1. As for all pivot mechanism, the mobile platform (PF) and the fixed base are interchangeable elements, i.e., swapping them maintains all kinematic properties of the mechanism, only the moments of inertia are affected.

2.1.2 Geometric Conditions

Condition 1: The quadrilaterals $OA_1B_1C_1$, $OA_2B_2C_2$ and $OA_3B_3C_3$ are geometrically similar (i.e., their corresponding angles are congruent, and their corresponding sides are proportional) but not reflected.

Condition 2: The quadrilaterals $C_1D_{11}D_{12}C_2$ and $C_2D_{21}D_{22}C_3$ are parallelograms.

2.1.3 Kinematic Properties

If Conditions 1 and 2 are respected, Type I pivots have a single degree of freedom (DOF) which is a pure rotation of the mobile platform (PF) around O. It is remarkable to note that, as long as singularities are avoided:

- The parasitic shift of the mobile platform is zero, independently of the amplitude of the rotation, as shown in Fig. 1d.
- The mechanism has no overconstraint and no internal DOF.
- The center of rotation can be located outside of the mechanism volume, which thus constitutes an RCM.

The pivot is said to be in *neutral* position when the lines drawn by B_1A_1, B_2A_2 and B_3A_3 all pass through O (e.g., as shown in Fig. 1e).
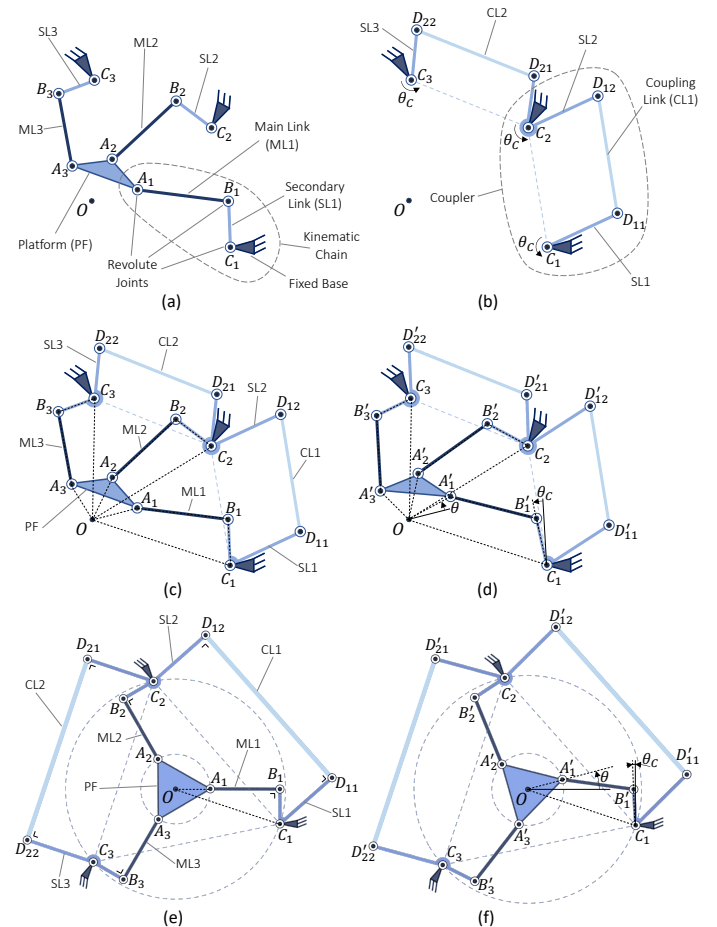

FIGURE 1: Type I pivot. (a) 3-RRR sub-mechanism (3-DOF). (b) Coupling sub-mechanism (1-DOF). (c) Type I Pivot satisfying only Conditions 1 and 2 in an arbitrary position. (d) Mechanism in (c) after rotation of an angle θ. (e) Type I pivot satisfying Conditions 1 to 7 in neutral position. (f) Mechanism in (e) after rotation of an angle θ. Video

animations of the mechanisms are available under the following link: https://vimeo.com/806278724 (Password: Quadrivot4-RRR).

2.1.4 Demonstration

Let's consider the sub-mechanism of Fig. 1a where the coupling links (CL1 and CL2) have been removed. This mechanism is a well know 3-RRR planar parallel structure with 3-DOF. If we force its mobile platform to rotate exactly around O (i.e., with the distances OA_1, OA_2 and OA_3 remaining constant), then the angles of the three central vertices $\angle C_1 O A_1$, $\angle C_2 O A_2$ and $\angle C_3 O A_3$ of the three quadrilaterals $OA_1B_1C_1$, $OA_2B_2C_2$ and $OA_3B_3C_3$ all vary by the same value θ. As a result, the three base vertex angles $\angle O C_1 B_1$, $\angle O C_2 B_2$ and $\angle O C_3 B_3$ all vary by the same angle θ_C.

We now consider the sub-mechanism of Fig. 1b where the mobile platform (PL) and the main links (ML1, ML2 and ML3) have been removed. It is a 1-DOF mechanism where Condition 2 stated above forces all the three base vertices C_1, C_2 and C_3 to rotate by the same angle θ_C during motion, since the parallel sides of parallelograms remain parallel. Therefore, this sub-mechanism fulfills the condition required by the sub-mechanism of Fig. 1a to obtain a pure rotation of the mobile platform (PF).

This proves the kinematic property stated above: indeed, when the two sub-mechanisms of Fig. 1a and Fig. 1b, which share the same secondary links SL1, SL2 and SL3, are connected to form the full structure of Fig. 1c, they constitute a pivot structure whose mobile platform rotates with no parasitic shift (see Fig. 1d).

2.1.5 Particular Cases

Some additional geometric conditions can be added to reach interesting cases:

Condition 3: In neutral position, the lines drawn by $C_1 B_1$ and $B_1 A_1$ (respectively $C_2 B_2$ and $B_2 A_2$, and $C_3 B_3$ and $B_3 A_3$) are orthogonal. Advantage: When rotating the platform in the vicinity of the neutral position, the rotation amplitude of the secondary links tends to zero. This minimizes the motion amplitude of the base revolute joints C_1, C_2 and C_3.

Condition 4: In neutral position, the line segment $D_{11}D_{12}$ is orthogonal to $C_1 D_{11}$ as well as to $C_2 D_{12}$ (respectively $D_{21}D_{22}$ is orthogonal to $C_2 D_{21}$ as well as to $C_3 D_{22}$). Advantage: the forces transmitted through the coupling links are minimized.

Condition 5: The distances OA_1, OA_2 and OA_3 are equal. When combined to Condition 1, Condition 5 implies that the quadrilaterals $OA_1B_1C_1$, $OA_2B_2C_2$ and $OA_3B_3C_3$ are geometrically congruent but not reflected. Advantage: symmetrical design.

Condition 6: The base pivots C_1, C_2 and C_3 are located with a rotational symmetry around O. Advantage: symmetrical design.

Condition 7: The distances $C_1 D_{11}$ and $C_2 D_{21}$ are equal. Advantage: the coupling chains have the same proportions, which improves the symmetry of the design.

A Type I pivot satisfying all the listed conditions (1 to 7) is shown in neutral position and in rotated position respectively in Figs. 1e and 1f.

2.1.6 Quasi-Type I Pivots

Design alternatives to Type I pivots, called Quasi-Type I pivots, where Conditions 1 and 2 are not fully respected, are presented due to their additional benefits. This new subgroup of the n-RRR Pivot family does however only approximate the kinematic properties of Type I pivots (see Section 2.1.3). The considered design variants, are listed below:

Mirrored kinematic chain: Condition 1 is modified to obtain two mirrored kinematic chains. This symmetry allows the structure to obtain symmetrical behaviors when the pivot is rotated clockwise and counterclockwise.

Watt's linkage coupler: In order to couple two mirrored kinematic chains, Condition 2 must be modified: the parallelogram linkage coupler (i.e., formed by the quadrilaterals $C_1 D_{11} D_{12} C_2$ or $C_2 D_{21} D_{22} C_3$), see Fig. 1b, is replaced by a Watt's linkage. This fulfills the coupling of the mirrored secondary links, forcing them to rotate with approximately equal angle magnitude, but in opposite directions. Since Conditions 1 and 2 are no longer respected, this leads to small parasitic shifts of the instant center of rotation for small rotation amplitudes. This parasitic shift is minimized if Condition 4 is respected. Note that the advantage of transmitting minimalized forces through the coupling links is also preserved with Condition 4.

Supernumerary kinematic chains: The number n of base pivots and respective kinematic chains ($n = 3$ in the case of Type I pivots) can be increased. This can lead to increased load capacity in out-of-plane directions.

Supernumerary coupling links: The number m of coupling links ($m = 2$ in the case of Type I pivots) can be increased. Note that additional coupling links (i.e., $m > 2$) induce overconstraints but lead to increased load capacity in radial directions.

2.2 Generic Type II Pivots

Type II pivots have the same topology as Type I pivots (see Fig. 2). Condition 1 is however different: the quadrilaterals $OA_1B_1C_1$, $OA_2B_2C_2$ and $OA_3B_3C_3$ are parallelograms (instead of similar polygons for Type I). Geometrically, this implies that $\theta = \theta_C$. Note that these parallelograms do not need to be similar, which was a constraining condition for Type I. If Condition 2 is respected, the geometric properties of Type I stated in Section 2.1.3 (i.e., zero parasitic shift, no under- or overconstraints and the possibility of obtaining an RCM) are also valid for Type II.
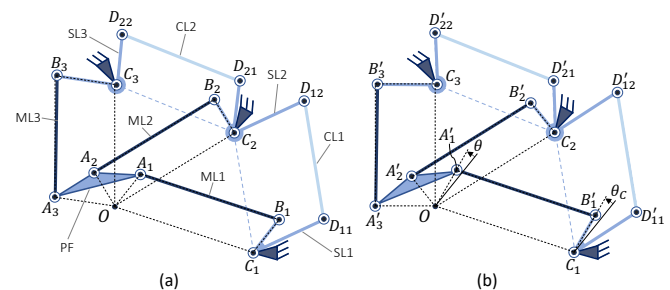

FIGURE 2: Type II pivot. (a) in an arbitrary position and (b) rotated by an angle θ

Since the parallelogram kinematic chains of Type II pivots can have independent shapes (see Fig. 2a), these pivots do not have a defined neutral position. The particular cases, variants and respective advantages of Type I (Section 2.1.5) are not applicable for Type II. For this reason, Type II is not further explored in this paper.

2.3 Selected n-RRR Pivot Architectures

We designed three n-RRR Pivot structures, all based on Quasi-Type I pivots. They are called TRIOVOT (3-RRR Pivot), QUADRIVOT (4-RRR Pivot) and HEXAVOT (6-RRR Pivot). These pivots have the advantage over the Type I pivots (Fig. 1) to be rotationally symmetrical, and thus rotate around the center O without parasitic shift. Indeed, in these arrangements, symmetry cancels the parasitic shift of Quasi-Type I pivots and moreover produces isotropic radial behaviors (e.g., radial stiffness) which contributes to keeping the center of mass of the pivot precisely at the center O when rotated under gravity.

2.3.1 TRIOVOT Mechanism

The TRIOVOT mechanism (Fig. 3) satisfies Conditions 1 to 7 of Type I pivots but uses an extra coupling link CL3 connecting the secondary links SL1 and SL3 via two additional revolute joints D_{31} and D_{32}, arranged symmetrically with respect to D_{11} and D_{12} and D_{21} and D_{22}.
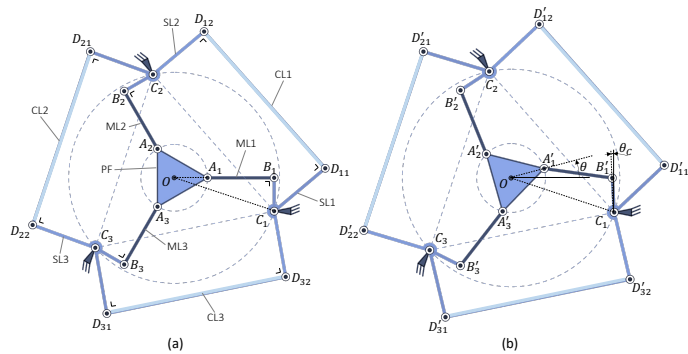

FIGURE 3: TRIOVOT mechanism (a) in neutral position and (b) rotated by an angle θ

2.3.2 QUADRIVOT Mechanism

The QUADRIVOT mechanism (Fig. 4) is a quasi-Type I pivot variant with $n = 4$ mirrored kinematic chains and $m = 4$ Watt's linkage couplers. It satisfies the following conditions:
- Condition 1, except that adjacent similar quadrilaterals are mirrored.
- Condition 3 for the 4 kinematic chains.
- Condition 4 for the 4 Watt's linkage couplers.
- Conditions 5 and 6 (rotational symmetry of order 2).

This arrangement has the advantage of having a rotational symmetry of order 2 and a symmetrical kinematic behavior in clockwise and counterclockwise directions, which is neither the case for the Type I pivots, nor for the TRIOVOT.
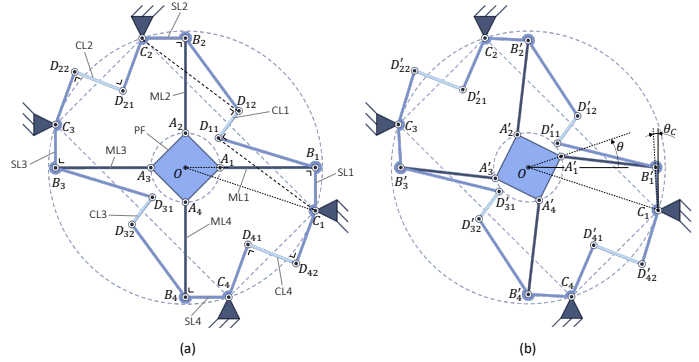

FIGURE 4: QUADRIVOT mechanism (a) in neutral position and (b) rotated by an angle θ

2.3.3 HEXAVOT Mechanism

The HEXAVOT mechanism (Fig. 5) is a quasi-Type I pivot variant with $n = 6$ mirrored kinematic chains and $m = 3$ Watt's linkage couplers. It satisfies the following conditions:
- Condition 1, except that adjacent similar quadrilaterals are mirrored.
- Condition 3 for the 6 kinematic chains.
- Condition 4 for the 3 Watt's linkage couplers.
- Conditions 5 and 6 (rotational symmetry of order 3).
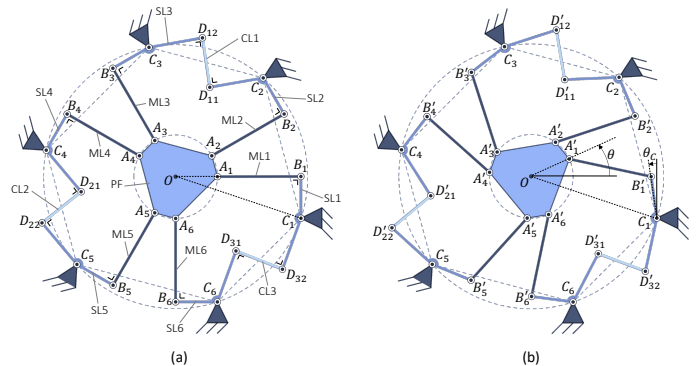- Condition 7 for the 3 Watt's linkage couplers, thus all the couplers are identical.

FIGURE 5: HEXAVOT mechanism (a) in neutral position and (b) rotated by an angle θ

3. FLEXURE IMPLEMENTATIONS

In this section, we provide flexure implementations of the TRIOVOT, QUADRIVOT and HEXAVOT, see Fig. 6. For all these flexure pivots, the main links and respective extremity revolute joints are each embodied by long leaf springs, called *main flexures*. The base revolute joints are implemented by Remote Center of Compliance (RCC) pivots, called *secondary flexures*. The revolute joints at the extremities of the coupling links are replaced by two leaf springs, called *coupling flexures*. As opposed to the QUADRIVOT and the HEXAVOT, the TRIOVOT possesses a rigid connecting rod, called *coupling connecting rod*, placed in-between the two coupling flexures. Since the fixed frame and platform are interchangeable (see Remark 1), the inner rigid platform of the pivot is called the *inner*

body and the outer rigid part connecting all the secondary flexures is called the *outer body*. The other rigid parts of the flexure pivots keep the same name as their corresponding kinematic architectures illustrated in Figs. 3-5.

Remark 2. Note that, even if each flexure has small parasitic shift defects, the rotational symmetry of the flexure pivots ensures that they rotate theoretically without parasitic center shift.

Mockups of the TRIOVOT, QUADRIVOT and HEXAVOT were fabricated in polyoxymethylene (POM) using a laser cutting machine to qualitatively verify the behaviors of these new designs. The dimensions of these demonstrators are given in Table 1. The flexure pivots show no visible parasitic shift when manually rotated (Fig. 7). Furthermore, the support stiffness seems high when applying radial loads by hand. Since the center shifts are very small and because POM tends to creep under external loads, we did not record any experimental data of parasitic center shift or radial stiffness. Instead, numerical characterization of these designs is performed in Section 4, using FEM modeling.
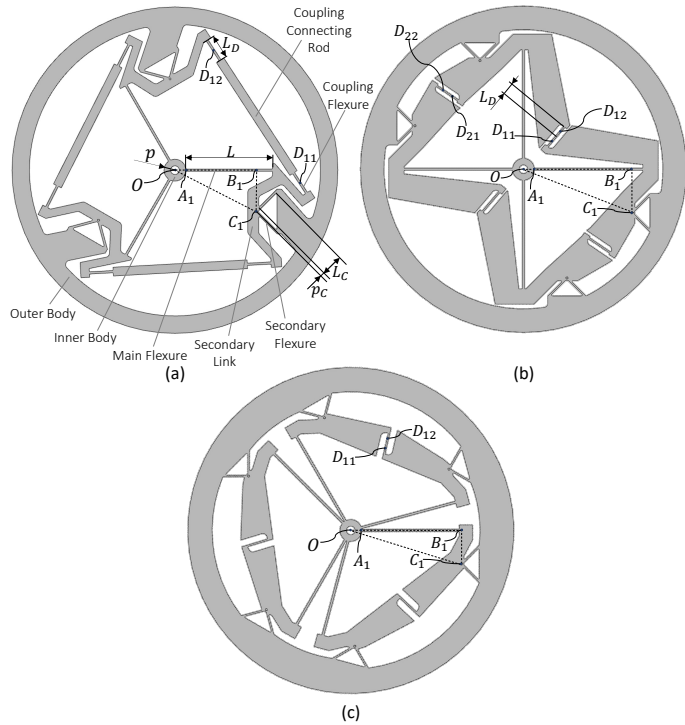

FIGURE 6: Flexure implementation of (a) the TRIOVOT, (b) the QUADRIVOT and (c) the HEXAVOT. The flexure pivots are all presented at equilibrium position (i.e., undeformed).

4. FEM PERFORMANCE COMPARISON WITH STATE-OF-THE-ART PLANAR FLEXURE PIVOTS

In order to highlight the advantages of the new flexure pivots presented in this paper (i.e., the TRIOVOT, the QUADRIVOT and the HEXAVOT), we compare their mechanical properties with two existing planar flexure pivots with minimized parasitic shift, namely the co-RCC [14] and the TRIVOT [19].

FIGURE 7: Mockups (POM, outer diameter of 150 mm) of (a) the TRIOVOT, (b) the QUADRIVOT and (c) the HEXAVOT. The inner body is attached to a fixed frame and the outer body is manually rotated.

4.1 Design Constraints

In order to ensure that the results are comparable, some parameters are fixed or optimized:

- Every pivot is made of POM, with a Young's modulus of $E = 3$ GPa.
- The outer body is identical (disc with an external diameter of 150 mm) to constrain the pivot size to a maximum allowed volume.
- The inner body radius is limited to $p \geq 5$ mm.
- The out-of-plane width b of the pivots is 5 mm.
- The thickness of the main and secondary flexures, respectively h and h_c, is 1 mm.
- Since the radial stiffness is highly dependent on the stiffness of the secondary and coupling flexures, they are dimensioned such that they have the same contribution to the rotation stiffness nonlinearity. In other words, the ratio K_2/K_0 (where the moment-angle characteristics of the pivot is given by $M_\theta = K_0\theta + K_1\theta^2 + K_2\theta^3 + \mathcal{O}(\theta^4)$) is set close to 2 rad^{-2} for all pivots.
- The length of the main flexures L must be as high as possible (respecting the allowable volume) to minimize the internal stress and maximize the angular stroke, see Eqs. (19) and (20).

Using these constraints, the TRIOVOT, the QUADRIVOT and the HEXAVOT are designed using the analytical model presented in Appendix A. The co-RCC and the TRIVOT are

respectively designed using Refs. [14] and [19]. The resulting dimensions are summarized in Table 1.

TABLE 1: Design parameters of the flexure pivots

Dimensions in mm	Main Flexures					Secondary Flexures			Coupling Flexures	
	L	h	p	e	r	L_C	h_C	p_C	L_D	h_D
co-RCC [14]	50	1	6	-	-	17	1	-	-	-
TRIVOT [19]	45	1	5	-	-	20	1	-	17.5	1
TRIOVOT	40	1	5	-7.5	19	10	1	2	11	1
QUADRIVOT	50	1	5	-5	20	13.5	1	2	6	0.75
HEXAVOT	45	1	5	1	15.5	14	1	1.5	5	0.75

4.2 FEM Model

To obtain the characteristics of the different pivots, two 2D nonlinear static FEM studies are carried out using the Solid Mechanics module of COMSOL Multiphysics 6.0:

Study 1: A rotation is applied to the outer body while the inner body is fixed (Fig. 8). The angle θ is varied from -20 deg to 20 deg with equal steps of 0.1 deg. The stiffness constant K_0 and nonlinear terms K_1 and K_2 are then obtained by fitting a 10th degree polynomial to the torque-angle relationship. The absence of over- and underfitting is verified. During this study, we also evaluate the maximum von Mises stress σ_{max} and the maximum parasitic center shifts Δx_{max} and Δy_{max} along the x and y axes, respectively.

Study 2: A small radial displacement (0.2 mm) is applied along x, then along y, to the outer body, whose rotation is constrained to the neutral orientation, while the inner body is fixed. The reaction forces are extracted in order to compute the respective radial stiffnesses K_x and K_y. We also verify that the structures do not buckle to ensure that the radial stiffness corresponds to the linear deformation of the flexures.

For both studies, the pivots are meshed with quadrilateral shell elements such that all flexures have 4 elements distributed over their thickness and at least 50 elements along their length.

5. RESULTS AND DISCUSSION

The results of the FEM comparison are presented in Tables 2 and 3. The pivots are compared in terms of rotation stiffness nonlinearity, parasitic center shift, radial stiffness magnitude and internal stress. The analytical model is also verified by comparing the theoretical and FEM data.

5.1 Moment-Angle Characteristics

The moment-angle characteristics of the different flexure pivots obtained from Study 1 is presented in Table 2 by providing the stiffness constant K_0 and nonlinearities K_1 and K_2. As can be seen from the data, the value of K_0 is proportional to

the number of kinematic chains n and inversely proportional to the length of the main flexures. For instance, the stiffness constant of the HEXAVOT is considerably higher due to its $n = 6$ kinematic chains. Additionally, even though the TRIOVOT and the QUADRIVOT have a different number of kinematic chains ($n = 3$ and $n = 4$ respectively), their stiffness constant is almost equal. This is because the TRIOVOT has significant shorter main flexures for a given diameter size due to its coupling connecting rods requiring considerable radial space, see Fig. 6a.
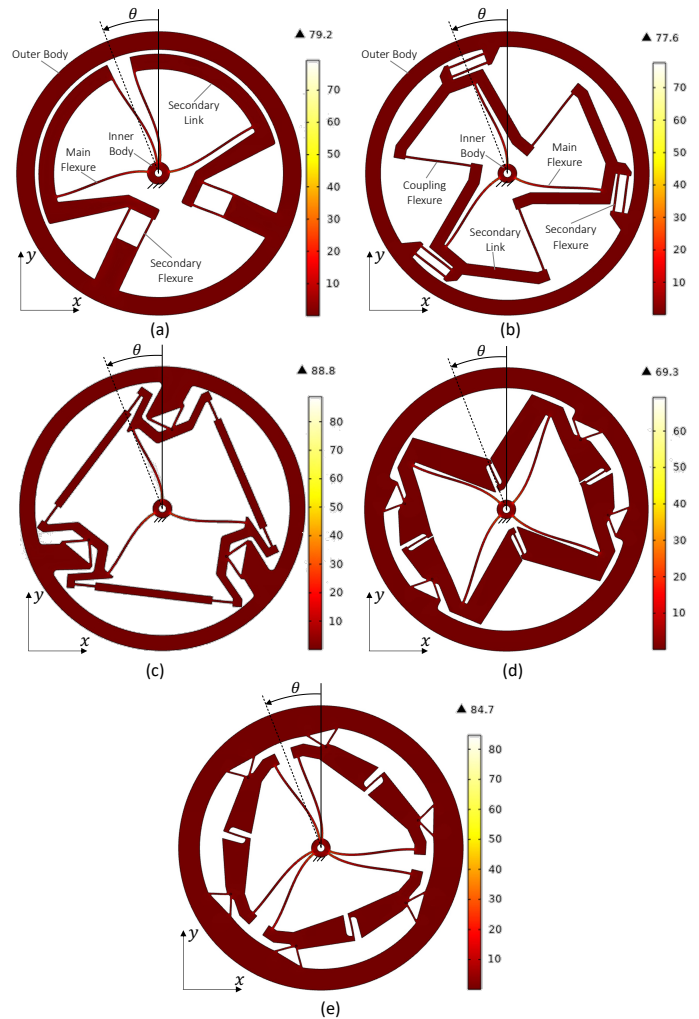

FIGURE 8: FEM simulation of (a) the co-RCC, (b) the TRIVOT, (c) the TRIOVOT, (d) the QUADRIVOT and (e) the HEXAVOT rotated by an angle of 20 deg. The color bars give the von Mises stress in MPa.

Since the stiffness constant K_0 is not the same between the pivots, we normalize the quadratic and cubic stiffness nonlinearities, respectively K_1 and K_2, by K_0, to make their effects comparable. It can be observed that the TRIOVOT has a large quadratic stiffness nonlinearity ratio K_1/K_0 in comparison to the other studied flexure pivots where this value is negligeable. This can be explained by the fact that the deformation of the TRIOVOT's main flexures strongly differs in CW and CCW rotation directions due to the orientation of the

kinematics chains ($n_{\text{CW}} = 3$ and $n_{\text{CCW}} = 0$, see Appendix A3). From Eqs. (10) and (17), obtaining $K_1 = 0$ is theoretically possible for the TRIOVOT, but this complicates the design significantly. For the QUADRIVOT and the HEXAVOT, K_1 is analytically null regardless of the main flexure dimensions because these flexure pivot structures have the same number of kinematics chains oriented CW and CCW ($n_{\text{CW}} = n_{\text{CCW}}$ in Eq. (17)). This is confirmed by the negligible values obtained by FEM.

As specified in Section 4.1, the cubic stiffness nonlinearity ratio K_2/K_0 of all the flexure pivots is close to 2 rad^{-2} targeted using the analytical model of Appendix A. Bear in mind that this model is based on linear beam theory, which is valid for small deformations, while the FEM results were obtained for larger deformations (±20 deg). This can explain some of the difference between both types of results. Nevertheless, a good agreement is observed overall between the analytical model and FEM results for the values of K_0 and K_2, and the order of magnitude of the K_1/K_0 ratio. This demonstrates the effectiveness of the analytical model for the preliminary dimensioning of such pivots, but FEM analysis is recommended for an accurate characterization of the flexure pivots at higher deformations.

Remark 3. To specific conditions, the quadratic and cubic stiffness nonlinearities (i.e., K_1 and K_2 respectively) can be set to zero (see Eqs. (17) and (18)). In this case and if the flexure pivots are used as time base oscillators, their isochronism defect is therefore minimized [14]. Alternatively, K_2 can be set to a specific value to compensate for externally induced isochronism defects (such as the ones introduced by escapements or if the oscillating balance wheel has a varying inertia) [11,28].

TABLE 2: Flexure pivot angular stiffness and maximum stress obtained from the analytical model (AM) and the simulations (FEM)

	Angular Stiffness						Maximum Stress	
	K_0 (Nmm/rad)		K_1/K_0 (rad^{-1})		K_2/K_0 (rad^{-2})		$\sigma_{\max}$ (MPa)	
	AM	FEM	AM	FEM	AM	FEM	AM	FEM
co-RCC [14]	561.3	540.1	-	0.002	-	2.08	49.4	79.2
TRIVOT [19]	456.8	431.0	-	0.009	-	2.26	54.3	77.6
TRIOVOT	533.2	519.7	-0.14	-0.23	2.13	1.97	63.4	88.8
QUADRIVOT	532.0	522.3	0	-9.5×10^{-5}	2.08	2.08	49.9	69.3
HEXAVOT	913.6	886.6	0	6.0×10^{-5}	2.35	2.31	57.8	84.9

5.2 Maximum Stress

The maximum value of the von Mises stress obtained with Study 1 is provided in Table 2. As expected, the maximum stress is situated at the beam extremity connected to the inner body (see Fig. 8) and is obtained at the maximum amplitude (i.e., ±20 deg).

It can be noticed that the stress is consistently higher in the FEM data than in the analytical results (increase of ~40%). A safety factor should thus be considered when designing such flexure pivots for a specified angular stoke using the analytical model.

The QUADRIVOT has the lowest maximum stress compared to all the other studied pivots. This also means that the QUADRIVOT has the maximum angular stroke.

5.3 Parasitic Center Shift

The FEM results of the parasitic center shift are given in Table 3 as the maximum deviation along x and y when performing Study 1. We can observe that the parasitic center shifts $\Delta x_{\max}$ and $\Delta y_{\max}$ are extremely small (a few nanometers for a pivot external diameter of 150 mm) for all the flexure pivots except the co-RCC (a bit less than a millimeter for the same pivot size). This shows the advantage of basing the design of flexure pivots on kinematic architectures with zero parasitic center shift, which is the case for all considered architectures except the co-RCC.

TABLE 3: Flexure pivot parasitic shift and radial stiffness obtained from the FEM model

	Maximum Parasitic Shift		Normalized Radial Stiffness	
	$\Delta x_{\max}$ (mm)	$\Delta y_{\max}$ (mm)	K_x/K_0 (mrad/mm²)	K_y/K_0 (mrad/mm²)
	FEM	FEM	FEM	FEM
co-RCC [14]	0.238	0.174	35.5	10.8
TRIVOT [19]	2.0×10^{-6}	2.7×10^{-6}	16.9	16.9
TRIOVOT	2.7×10^{-6}	3.0×10^{-6}	134.3	134.1
QUADRIVOT	5.8×10^{-7}	4.4×10^{-7}	292.3	293.6
HEXAVOT	1.8×10^{-6}	2.4×10^{-6}	218.5	218.3

5.4 Radial Stiffness

The FEM data of the radial stiffness K_x and K_y (Study 2) are provided in Table 3. For comparison purposes, these values are normalized by the angular stiffness constant K_0 of the respective flexure pivots. As opposed to the co-RCC having a large anisotropy defect ($K_x \cong 3.3K_y$), the other flexure pivots have all a radial stiffness which is rather isotropic thanks to their rotational symmetry.

The normalized radial stiffness is maximum for the QUADRIVOT. Indeed, the average of K_x/K_0 and K_y/K_0 is 1.3, 2.2, 13 and 17 times higher for the QUADRIVOT compared to the HEXAVOT, the TRIOVOT, the co-RCC and the TRIVOT, respectively.

We assume that the HEXAVOT has a lower normalized radial stiffness than the QUADRIVOT because it has less couplers and more kinematic chains. The support stiffness reduction in the radial directions of the TRIOVOT could be

attributed to its long coupling connecting rods which can deform axially. This decreases the coupling efficiency and thus reduces the blocking of the translational motions along x and y of the pivot. The low radial stiffness of the co-RCC is attributed to the lack of parallel kinematics chains between the inner and outer bodies. Finally, the lower radial stiffness of the TRIVOT structure can be explained by the fact that the force transmitted from one secondary link to another is strongly misaligned with the axis of its coupling flexures, reducing drastically the coupling efficiency. In contrast, for the selected n-RRR Pivot structures, the force transmitted in the coupling flexures is aligned with their axis due to Condition 4. This efficient coupling of the kinematic chains appears to greatly increase the radial stiffness.

6. CONCLUSION

The new n-RRR Pivot family introduced in this article leads to two kinds (Type I and Type II) of exact zero parasitic shift pivoting kinematic structures. Based on this generic invention, we designed three symmetrical kinematic variants (TRIOVOT, QUADRIVOT and HEXAVOT) approaching the geometric properties of the exact Type I and proposed flexure-based implementations. We confronted the performance of these novel flexure pivots with equivalent planar flexure pivots from the state of the art (TRIVOT and co-RCC) having the same volume (150 mm diameter, 5 mm height), same minimal blade thickness (1 mm), same material (POM) and same angular stiffness nonlinearity. The comparison which was based on FEM models covered the parasitic shift, the admissible angular stroke and the radial stiffness. In summary the newly introduced flexure pivots are all 8 to 13 times radially stiffer than the considered pivots from the state of the art, while having zero parasitic shift properties and equivalent angular strokes.
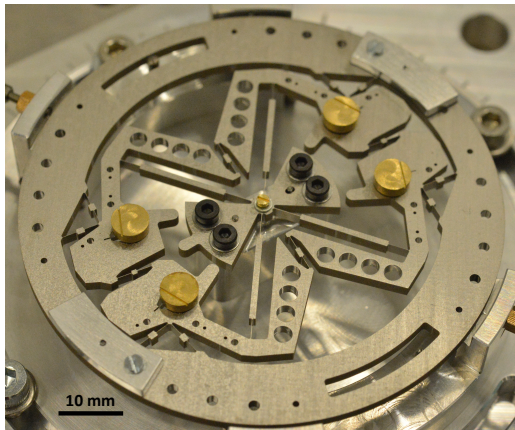

FIGURE 9: QUADRIVOT time base oscillator (titanium alloy) ready for experimental testing

Our future work will focus on experimentally validating the designs presented in this article. A large-scale TiAl4V6 (75 mm diameter) flexure-based rotating oscillator prototype based on the QUADRIVOT structure was built for this purpose (Fig. 9). Subsequent research will include the miniaturization of this mechanism and its fabrication in monocrystalline silicon for integration in mechanical wristwatches. A large spectrum of other applications such as optomechanical systems for aerospace applications, RCM mechanisms for MIS robotics or micro- and nanopositioning systems are also foreseen.

APPENDIX A: ANALYTICAL MODEL

This Appendix introduces the generic theoretical model used to design all the flexure pivots described in Section 3. For the calculations, we consider that all kinematic chains of a given flexure pivot have the same dimensions and deforms equally. Therefore, we first consider the rotation stiffness of a single main flexure (Section A1), then of the secondary and coupling flexures (Section A2), to finally compute the nonlinear moment-angle relationship of a whole flexure pivot based on its number of kinematic chains and coupling links (Section A3). The admissible stroke of the flexure pivot is also evaluated (Section A4).

A1 Rotation Stiffness of the Main Flexures

Figure 10 illustrates the deformation and the load case of one of the main flexures. Each consists of an initially straight slender beam hinged at two pivot joints at O (main pivot) and at C (secondary pivot). The main pivot (virtual) corresponds to the rotation of the whole flexure pivot. The secondary pivot represents the rotation of the secondary flexure. Since the stiffness of the secondary flexures will be considered in Section A2, no restoring torque is applied to the secondary pivot at point C in Fig. 10. At equilibrium (Fig. 10a), the beam axis is horizontal and intersects the center O. The distance between O and the left extremity of the beam is denoted p. The horizontal and vertical distances between the right extremity of the beam and the center C are named e and r, respectively. As opposed to the beam, the links (i.e., the platform and the secondary link) are considered rigid. In Fig. 10b, the main pivot is rotated by an angle θ when a moment $M_{\theta,1\text{beam}}$ is applied to it. Due to the beam shortening along the horizontal axis, the secondary pivot rotates by an angle θ_C. The beam deflection $y(x)$ and the reaction forces P and V, respectively along x and y, and the bending moment M are illustrated in Fig. 10c.

To obtain simple closed-form solutions of the beam deflection, the impact of the axial force P on the beam curvature is neglected and considering small deformations, the Euler-Bernoulli equation gives:

$$M(x) = EIy''(x) = M_0 + Vx \qquad (1)$$

where EI is the flexural rigidity of the beam. Applying the boundary conditions $y(0) = 0$, $y'(0) = \theta$, $y'(l) = \theta_C$ and

$y(l) = -p(\theta - \theta^3/6) - e\theta_C$ based on small-angle approximations and solving the differential equation (1), the beam deflection becomes:

$$y(x) = \theta x + \frac{M_0}{EI}\frac{x^2}{2} + \frac{V}{EI}\frac{x^3}{6} \qquad (2)$$

where:

$$M_0 = \frac{EI\left(p\theta^3 - 2(2l+3p)\theta - 2(l+3e)\theta_C\right)}{l^2} \qquad (3)$$

$$V = \frac{2EI\left(-p\theta^3 + 3(l+2p)\theta + 3(l+2e)\theta_C\right)}{l^3} \qquad (4)$$
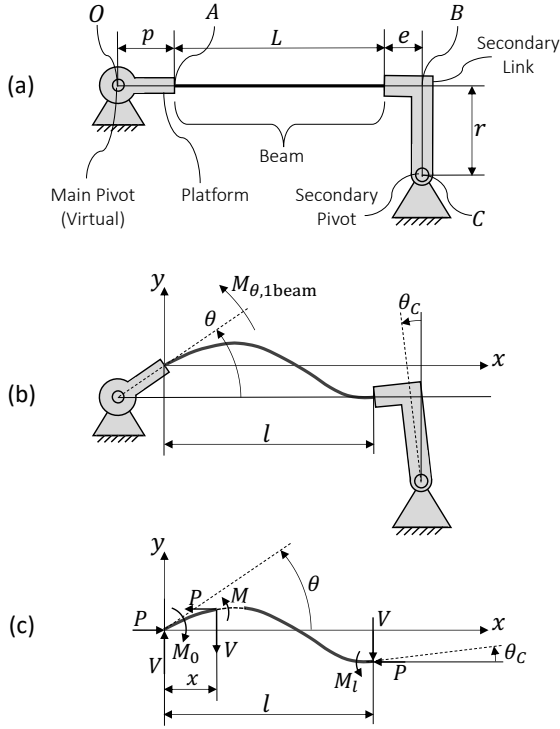

FIGURE 10: (a) As-fabricated, (b) deformed and (c) free-body diagram of one of the main flexures

The axial load P can be derived using the boundary condition of the bending moment at the right beam extremity $M(l) = M_l = -P(r - e\theta_C) - V(e + r\theta_C)$:

$$P = -\frac{V(e+l+r\theta_C)+M_0}{(r-e\theta_C)} \qquad (5)$$

The secondary pivot rotation θ_C is related to the beam shortening $\Delta l = L - l$ which can be approximated by:

$$\Delta l = \int_0^l \frac{\left(y'(x)\right)^2}{2}dx = -p\frac{\theta^2}{2} + r\theta_C - e\frac{\theta_C^2}{2} \qquad (6)$$

Substituting the differentiation of Eq. (2) in Eq. (6), we can obtain the relation between the main pivot and the secondary pivot using series expansions around $\theta = 0$ up to the third order:

$$\theta_C = \frac{1}{15}\frac{1+9\bar{p}+9\bar{p}^2}{\bar{r}}\theta^2$$
$$- \frac{1}{450}\frac{(1-3\bar{e}-3\bar{p}-36\bar{e}\bar{p})(1+9\bar{p}+9\bar{p}^2)}{\bar{r}^2}\theta^3 + \mathcal{O}(\theta^4) \qquad (7)$$

where $\bar{p} = p/l$, $\bar{e} = e/l$, $\bar{r} = r/l$.

The moment applied to the main pivot is obtained from the reaction forces and moment at the left beam extremity and by substituting Eq. (7) in Eqs. (3-5):

$$M_{\theta,1\text{beam}} = -M_0 + Vp\left(1 - \frac{\theta^2}{2}\right) - Pp\theta =$$
$$K_{0,1\text{beam}}\theta + K_{1,1\text{beam}}\theta^2 + K_{2,1\text{beam}}\theta^3 + \mathcal{O}(\theta^4) \qquad (8)$$

where:

$$K_{0,1\text{beam}} = 4\frac{EI}{L}(1 + 3\bar{p} + 3\bar{p}^2) \qquad (9)$$

$$K_{1,1\text{beam}} = \frac{2}{15}\frac{EI}{L}\frac{(1+24\bar{p}+9\bar{p}^2)(1+3\bar{e}+3\bar{p}+6\bar{e}\bar{p})}{\bar{r}} \qquad (10)$$

$$\begin{aligned}K_{2,1\text{beam}} = \frac{1}{225}\frac{EI}{L}\frac{1}{\bar{r}^2}(&-1 + 9\bar{e}^2 \\ &+ 3(17 + 76\bar{e} + 129\bar{e}^2 - 300\bar{r}^2)\bar{p} \\ &+ 9(60 + 242\bar{e} + 339\bar{e}^2 - 200\bar{r}^2)\bar{p}^2 \\ &+ 27(23 + 118\bar{e} + 174\bar{e}^2)\bar{p}^3 \\ &+ 81(1 + 14\bar{e} + 24\bar{e}^2)\bar{p}^4)\end{aligned} \qquad (11)$$

It can be observed that the stiffness of one main flexure has nonlinear terms (e.g., quadratic and cubic nonlinearities $K_{1,1\text{beam}}$ and $K_{2,1\text{beam}}$, respectively) in addition to the stiffness constant $K_{0,1\text{beam}}$.

A2 Stiffness Contribution of the Secondary and Coupling Flexures

Unlike the main flexures, the secondary and coupling flexures are modeled using the pseudo-rigid body model [29], i.e., their rotation stiffness is assumed constant. This is justified by the fact that their motion is of second order of the rotation of the pivot and hence their contribution is significantly smaller, see Eq. (7). As explained in Section 2, a coupler can be either a parallelogram or a Watt's linkage, see Fig. 11. Assuming small deformations, we consider that the respective rotation magnitudes are equal (i.e., $\theta_{C,1} = \theta_{C,2} = \theta_C$). Then, the deformation angles of the coupling and secondary flexures are also the same. Since there are one secondary flexure per kinematic chain and two coupling flexures per coupler, it follows that the strain energy of the couplers given for n kinematic chains and m coupling links is:

$$E_{\text{strain,couplers}} = \frac{n}{2}K_C\theta_C^2 + mK_D\theta_C^2 \qquad (12)$$

where K_C and K_D stand for the angular stiffness constant of the secondary and coupling flexures, respectively. The moment applied by the secondary and coupling flexures to the flexure pivot rotation is computed by differentiating Eq. (12) by the pivot angle θ and substituting Eq. (7):

$$M_{\theta,\text{couplers}} = \frac{dE_{\text{strain,couplers}}}{d\theta} = K_{2,\text{couplers}}\theta^3 + \mathcal{O}(\theta^4) \qquad (13)$$

where:

$$K_{2,\text{couplers}} = \frac{2(nK_C+2mK_D)(1+9\bar{p}+9\bar{p}^2)^2}{225\bar{r}^2} \qquad (14)$$

As shown in Eq. (13), the secondary and coupling flexures bring a cubic stiffness nonlinearity to the flexure pivot rotation.

Remark 4. If the secondary flexure corresponds to an RCC pivot and the coupling flexure is a simple beam (as shown in Fig. 6), their respective angular stiffnesses are $K_C = 8EI_C(1 + 3p_C/L_C + 3(p_C/L_C)^2)/L_C$ and $K_D = EI_D/L_D$ (respectively Eqs. (5.6) and (3.1) in Ref. [30]).
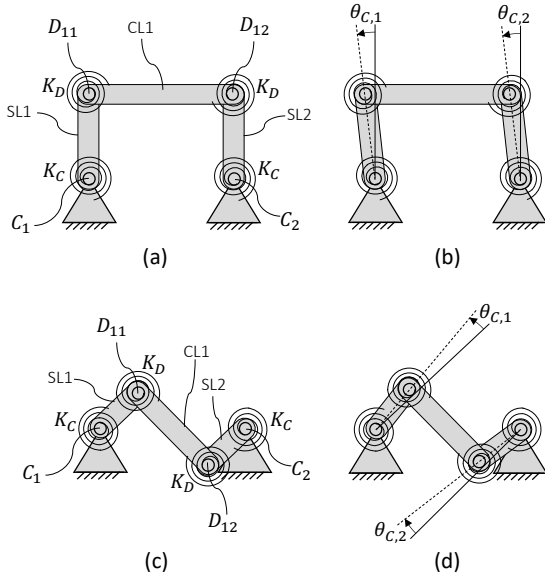

FIGURE 11: Pseudo rigid body model of the coupling of the secondary links by a parallelogram coupler in (a) rest and (b) deformed position or a Watt's linkage coupler in (c) rest and (d) deformed position

A3 Total Rotation Stiffness of the Flexure Pivot

Since each main flexure has a second order stiffness nonlinearity $K_{1,1\text{beam}}$, the total stiffness of the flexure pivot depends on the orientation of the kinematic chains. For instance, the kinematic chains of the TRIOVOT are all oriented CW (or all CCW), but the QUADRIVOT and HEXAVOT have the same number of kinematic chains that are oriented CW and CCW. We thus define n_{CW} and n_{CCW} as the number of main flexures oriented respectively as or as contrary to the main flexure

illustrated in Fig. 10. The total moment-angle relationship of a flexure pivot with n kinematic chains (note that $n = n_{\text{CW}} + n_{\text{CCW}}$) and m couplers is finally a weighted sum of the stiffnesses given in Eqs. (8) and (13):

$$M_\theta = n_{\text{CW}}M_{\theta,1\text{beam}}(\theta) - n_{\text{CCW}}M_{\theta,1\text{beam}}(-\theta)$$
$$+ M_{\theta,\text{couplers}} = K_0\theta + K_1\theta^2 + K_2\theta^3$$
$$+ \mathcal{O}(\theta^4) \qquad (15)$$

where:

$$K_0 = nK_{0,1\text{beam}} \qquad (16)$$

$$K_1 = (n_{\text{CW}} - n_{\text{CCW}})K_{1,1\text{beam}} \qquad (17)$$

$$K_2 = nK_{2,1\text{beam}} + K_{2,\text{couplers}} \qquad (18)$$

A4 Admissible Angular Stroke

Since the deformation of the secondary and coupling flexures is significantly smaller than that of the main flexures (θ_C is of second order with respect to θ), it is assumed that the maximum internal stress $\sigma_{\max}$ is observed in the main flexures and more specifically at the inner extremity of their beams (i.e., at the left extremity of the beam in Fig. 10). This assumption can be verified analytically (e.g., using Eq. (7)) or through FEM modeling, which was done in the case of the designs in this study (see Section 5.2). Substituting Eqs. (1) and (3) in the maximum stress equation of the main flexures yields:

$$\sigma_{\max} = \frac{|y''(0)|}{E}\frac{h}{2} = \frac{(2+3\bar{p})h}{El}\theta + \mathcal{O}(\theta^2) \qquad (19)$$

where E is the Young's modulus of the material and h is the thickness of the main flexure beams. The admissible angular stroke of the pivot $\theta_{\max}$, which corresponds to the maximum stroke of one of its main flexure beams, can be evaluated using Eq. (19):

$$\theta_{\max} = \frac{\sigma_{\text{adm}}l}{Eh(2+3\bar{p})} \qquad (20)$$

where σ_{adm} is the maximum engineering tolerated value of the stress that can be applied to the material (e.g., the yield or fatigue strengths).

Remark 5. Since we consider small beam deformations, the parameter l can be replaced by L in all the equations.

REFERENCES
[1] Marković, K., and Zelenika, S., "Characterization of Cross-Spring Pivots for Micropositioning Applications," *SPIE Microtechnologies*, Barcelona, Spain, 2015, p. 951727.
[2] Tissot-Daguette, L., Smreczak M., Baur, C., and Henein, S., "Load cell with adjustable stiffness based on a preloaded T-shaped flexure pivot," *Proceedings of the 21st*

international conference of the european society for precision engineering and nanotechnology, Copenhagen, Denmark, 2021, pp. 217–220.

[3] Smreczak, M., Tissot-Daguette, L., Thalmann, E., Baur, C., and Henein, S., "A load cell with adjustable stiffness and zero offset tuning dedicated to electrical micro- and nanoprobing", *Precision Engineering*, 76, 2022, pp. 208-225.

[4] Xu, Q., "Design and fabrication of a novel compliant rotary nanopositioning stage," *2013 IEEE International Conference on Robotics and Automation, Karlsruhe*, Germany, 2013, pp. 1415-1420.

[5] Tissot-Daguette, L., Baur, C., Bertholds, A., Llosas, P., and Henein, S., "Design and modelling of a compliant constant-force surgical tool for objective assessment of ossicular chain mobility," *2021 21st International Conference on Solid-State Sensors, Actuators and Microsystems (Transducers)*, IEEE, 2021, pp.1299–1302.

[6] Zanaty, M., Fussinger, T., Rogg, A., Lovera, A., Lambelet, D., Vardi, I., Wolfensberger, T.J., Baur, C., and Henein, S., "Programmable multistable mechanisms for safe surgical puncturing," *Journal of Medical Devices*, 13(2), 2019, p. 021002.

[7] Thomas, T. L., Kalpathy Venkiteswaran, V., Ananthasuresh, G. K., and Misra, S., 2021, "Surgical Applications of Compliant Mechanisms: A Review," *Journal of Mechanisms and Robotics*, 13(2), p. 020801.

[8] Seelig, F. A., "Flexural Pivots for Space Applications," *Proceedings of the 3rd Aerospace Mechanisms Symposium*, California Institute of Technology, USA, 1968.

[9] Spanoudakis, P., Kiener, L., Cosandier, F., Schwab, P., Giriens, L., Kruis, J., Grivon, D., Psoni, G., Vrettos, C., and Bencheikh, N., "Large angle flexure pivot development for future science payloads for space applications," *MATEC Web of Conferences*, 304, 2019, p. 07016.

[10] Fowler, R., Maselli, A., Pluimers, P., Magleby, S., and Howell, L., "Flex-16: A large-displacement monolithic compliant rotational hinge," *Mechanism and Machine Theory*, 82, 2014, pp. 203-217.

[11] Thalmann, E., "Flexure Pivot Oscillators for Mechanical Watches," Ph.D. thesis, EPFL, Lausanne, 2020.

[12] Robuschi, N., Braghin, F., Corigliano, A., Ghisi, A., and Tasora, A., "On the Dynamics of a High Frequency Oscillator for Mechanical Watches," *Mechanism and Machine Theory*, 117, 2017, pp. 276–293.

[13] Schneegans, H., Thalmann, E., and Henein, S., "Shaking Force Balancing of a 2-DOF Isotropic Horological Oscillator," *Precision Engineering*, 72, 2021, pp. 502–520.

[14] Thalmann, E., Kahrobaiyan, M., Vardi, I., and Henein, S., "Flexure Pivot Oscillator With Intrinsically Tuned Isochronism," *Journal of Mechanical Design*, 142(7), 2020, p. 075001.

[15] Wittrick, W., "The properties of crossed flexure pivots, and the influence of the point at which the strips cross," *Aeronautical Quarterly*, 2(4), 1951, pp. 272-292.

[16] Pei, X., Yu, J., Zong, G., Bi, S., and Hu, Y., "A Novel Family of Leaf-Type Compliant Joints: Combination of Two Isosceles-Trapezoidal Flexural Pivots," *Journal of Mechanisms and Robotics*, 1(2), 2009, p. 021005.

[17] Huo, T., Yu, J., Zhao, H., Wu, H., and Zhang, Y., "A family of novel RCM rotational compliant mechanisms based on parasitic motion compensation," *Mechanism and Machine Theory*, 156, 2021, p. 104168.

[18] Zhao H., and Bi S., "Accuracy characteristics of the generalized cross-spring pivot," *Mechanism and Machine Theory*, 45, 2010, pp. 1434–1448.

[19] Thalmann, E., and Henein, S., "Design of a Triple Crossed Flexure Pivot With Minimized Parasitic Shift," *Proceedings of the ASME 2021 International Design Engineering Technical Conferences and Computers and Information in Engineering Conference. Volume 8A: 45th Mechanisms and Robotics Conference (MR)*, Virtual, Online, 2021, p. V08AT08A003.

[20] Liu, L., Bi, S., Yang, Q., and Wang, Y., "Design and experiment of generalized triple-cross-spring flexure pivots applied to the ultra-precision instruments," *Review of Scientific Instruments*, 85(10), 2014, p. 105102.

[21] Henein, S., Spanoudakis, P., Droz, S., Myklebust, L., and Onillon, E., "Flexure pivot for aerospace mechanisms," *Proceedings of the 10th ESMATS*, San Sebastian, Spain, 2003, pp. 1-4.

[22] Thalmann, E., and Henein, S., "Triple Crossed Flexure Pivot Based on a Zero Parasitic Center Shift Kinematic Design," *Journal of Mechanisms and Robotics*, 14(4), 2022, p. 045001.

[23] Wiersma, D., Boer, S., Aarts, R., and Brouwer, D., "Design and Performance Optimization of Large Stroke Spatial Flexures," *Journal of Computational and Nonlinear Dynamics*, 9(1), 2014, p. 011016.

[24] Tissot-Daguette, L., and Henein, S., "Pivot, process for manufacturing such a pivot, oscillator comprising such a pivot, watch movement and timepiece comprising such an oscillator," Patent EP 22206404.0, Holder EPFL, 2022.

[25] Kuo, C.-H., Dai, J.S., and Dasgupta, P., "Kinematic design considerations for minimally invasive surgical robots: an overview," *The International Journal of Medical Robotics and Computer Assisted Surgery*, 8(2), 2012, pp. 127-145.

[26] Kahrobaiyan, M., Thalmann, E., Rubbert, L., Vardi, I., and Henein S., "Gravity-insensitive flexure pivot oscillators," *Journal of Mechanical Design*, 140 (7), 2018, p. 075002.

[27] Thalmann, E., Gubler, Q., and Henein, S., "Gravity-Compensation Design Approaches for Flexure-Pivot Time Bases," *Machines*, 10(7), 2022, p. 580.

[28] Thalmann, E., and Henein, S., "Design of a Flexure Rotational Time Base With Varying Inertia," *Journal of Mechanical Design*, 143, 2021, p. 115001.

[29] Howell, L., *Compliant Mechanisms*, Wiley, New York, 2001.

[30] Cosandier, F., Henein, S., Richard, M., and Rubbert, L., *The Art of Flexure Mechanism Design*, EPFL Press, Lausanne, 2017.